Use of lignocellulosic materials and 3D printing for the development of structured monolithic carbon materials

Ying Shao, Chamseddine Guizani, Philippe Grosseau, Didier Chaussy, Davide Beneventi

Use of Lignocellulosic Materials and 3D Printing for the Development of Structured Monolithic Carbon Materials

Ying SHAO[a,], Chamseddine GUIZANI[a], Philippe GROSSEAU[b], Didier CHAUSSY[a], Davide BENEVENTI[a,]*

[a]Univ. Grenoble Alpes, CNRS, Grenoble INP, LGP2, F-38000 Grenoble, France

[b]Ecole des Mines de Saint Etienne, Centre Sciences des Processus Industriels et Naturels (SPIN), 158 Cours Fauriel, CS 62632, F-42023 Saint Etienne, France

Abstract

In the present work, electrically conductive and mechanically resistant carbon structures were elaborated by 3D printing and subsequent pyrolysis using microfibrillated cellulose/lignosulfonate/cellulose powder (labeled as MFC/LS/CP) blends. The processability of MFC/LS/CP slurries by 3D printing was examined by rheological tests in both steady flow and thixotropic modes. The printed MFC/LS/CP pastes were self-standing, provided a high printing definition and were proved to be morphologically stable to air drying and the subsequent pyrolysis. Pyrolysis at a slow rate (0.2°C/min) to a final temperature ranging between 400 and 1200°C was used to manufacture MFC/LS/CP carbons. The TGA/DTG was applied to monitor the thermal degradation of MFC/LS/CP materials in blends as well as in a separated form. The resulting carbons were further characterized in terms of morphology, microstructure and physical properties (such as density, electrical conductivity and mechanical strength). At 900°C, MFC/LS/CP carbons displayed a high electrical conductivity of 47.8 S/cm together with a low density of 0.74 g/cm^3 and a porosity of 0.58. They also achieved an elastic modulus of 6.62 GPa. Such interesting electrical and mechanical properties would lead to a promising application of MFC/LS/CP-derived biocarbons in energy storage devices as electrode materials in close future.

*Corresponding author.
E-mail address: davide.beneventi@pagora.grenoble-inp.fr

Keywords: Bio-sourced material; 3D printing; Carbonization; Electrical conductivity; Energy storage device

1. Introduction

Over the last decade, additive manufacturing progressively evolved from the laboratory/ prototyping- to an industrial-process, capable of processing an ever increasing panel of structural and functional materials with various physical forms [1]-[3], i.e. from metallic/ceramic powders to food/biological hydrocolloids. Among available 3D printing technologies, paste/fused material extrusion emerged as one of the most versatile techniques for multi-material processing and it has been successfully used with carbon fiber-, carbon nanotubes- and graphene-reinforced polymer composites for both structural and electronic applications [4]-[6]. Indeed, the ability to combine materials with different functionalities in a single object paved the way to the additive manufacturing of new 3D printed structures embedding electronic devices [9]-[10]. Despite a relatively high conductivity (ranging from 0.01 to 4.76 S/cm [6]-[8]), carbon-polymer composites are adapted for the fabrication of resistive/antistatic patterns, whereas high conductivity silver-based conductive inks are the preferred system for the deposition of conductive paths and electrodes on insulating substrates. Thereafter, in most cases the fabrication of highly conducting 3D structures requires the combination of both conductive and structural materials [9]. In order to go beyond this limitation, the aim of this work was to manufacture monolithic carbon objects with both conductive and structural functionalities using 3D printing and lignocellulosic materials as carbon precursors. Lignocellulosic materials represent the most abundant polymer source in nature and have been widely used in medical, packaging, construction and energy industries. In energy storage devices, biomass was usually used as “inactive” component, such as binder in electrodes [11], reinforcing agent in gel-polymer electrolytes [11], separator [12] or nanoporous template in supercapacitors [13]. More recently, its carbonaceous chars, obtained

after pyrolysis in inert atmosphere, have been successfully applied as an “active” electrode materials [14]-[16], although no further interpretation concerning their development of electrical conductivity during pyrolysis was given.

Among few studies from the literature, Perepelkin [17] summarized an electrical resistivity decrease of nearly 12 orders of magnitude for biomass precursor heat-treated at 350°C and 950°C, despite the fact that biomass has been considered as non-graphitizing carbon precursor. McDonald-Wharry et *al.* [18] proposed a model called “distorted graphene triad” for describing the microstructure of non-graphitizing carbons. Such model is composed of 3 distinguish microstructures: regular graphite-like domains, distorted graphite regions and amorphous carbon phase. Rhim et *al.* [19] studied the electrical property development throughout the pyrolysis of microcrystalline cellulose (MCC) using a binary model (after compensation of porosity effect). The authors suggested that the increasing temperature leads to the continuous growth of conductive carbon clusters and upon a percolation threshold between 600 and 610°C with a conductive phase volume fraction of 0.39, conductive phases begin to make contact so that the DC conductivity become detectable. In addition to the improvement of electrical property by increased pyrolysis temperatures, Kercher et al. [20] also reported the temperature-strengthened mechanical properties by studying the carbonization of fiberboards.

In the midst of various lignocellulosic materials, microfibrillated cellulose (MFC) and lignosulfonate (LS) have caught special attention for the elaboration of carbon precursor composites [19][21]. MFC are released from cellulose fibers via mechanical treatments with potential chemical treatment[12]. Thanks to their micro-scaled dimensions, MFC forms a dense fiber network with high strength [23]. LS is a water-soluble macro-polymer composed of a large quantity of cross-linked aromatic cycles (lignin phenyl propane units substituted with sulfonate groups) [24]. It is an industrial byproduct from the production of wood pulp

using sulfite pulping. The composites elaborated from MFC/LS slurries are self-standing with MFC playing the role of mechanical reinforcement whereas LS ensures the carbon yield after pyrolysis (LS could achieve a high carbon yield up to 50% after 800°C, compared to the 21% for MFC and the 3% for CP) [25]-[26]. However, a previous work [25] revealed that adding LS into MFC hydrogels led to either a disruption of the hydrogels' stability after 3D printing due to lack of viscosity (with 10%-30% LS), or a loss of shape definition because of the long restauration time (with 50% LS). Since LS is an essential component to the composite due to its large contribution to the carbon yield [26] that is important to ensure the thermal stability and conductivity of as-elaborated bio-carbons, one solution to improving the hydrogels' printability while keeping using a large quantity of LS in the formulation is to add appropriate additives. Cellulose and its derivatives were characterized to have a high viscosity and shear-thinning property [27] in their water suspensions. Thereby, the commercial cellulose powder (CP) was chosen as the additive in this work.

A screw-pump based 3D printing technic was used as the principal forming method for elaborating MFC/LS/CP carbon precursor, owing to the fact that all pristine materials are water-processable and could form appropriate hydrogel for printing. The interest of using 3D printing in this work mainly consists in its flexibility to produce samples in various forms and dimensions in order to meet different characterization purposes. For instance, as the simplest form, monolines were printed only for tensile tests. More excitingly, electrodes could be directly printed using a two-head printer with one head firstly printing a web-like structure then another filling the web holes with other types of hydrogel (probably electrochemistry-strengthen components). As a result, 3D printing not only amplifies the potential applications of MFC/LS/CP as a printable hydrogel but also proposes an unexplored way to elaborate electrodes of next generation.

In addition to the thermal stability [28], biomass-derived carbons could acquire important porosity [29], interesting electrical property and mechanical strength with regard to their comparatively low density [30], making them a promising materials for electrodes in energy storage devices [31]. In the current work, the MFC/LS/CP hydrogel was firstly examined in hydrogel rheology. Later, the "green" carbons from MFC/LS/CP precursor were elaborated using 3D printing with subsequent pyrolysis and were characterized in terms of thermal stability, morphology, mechanical strength, electrical conductivity and microstructure evolution.

2. Materials and methods

2.1 Materials and hydrogel preparation

2% (w/w) MFC hydrogel was provided by FCBA (Saint Martin d'Hères, France). It was produced from bleached hardwood (birch) kraft pulp via a mechano-enzymatic protocol along with subsequent homogenization at high pressure. Sodium lignosulfonate (NaLS or simply LS) was purchased from Carl Roth GmbH + Co. KG (France).It is in the form of a brown powder with a sodium content reaching 9%. The elementary analysis of used MFC and LS could be found in a previous work [26]. High purity cellulose powder (CP) from cotton was purchased from Sigma-Aldrich (France) with a nominal particle size of 50 µm. All three materials were used as received.

Hydrogel was prepared by adding LS and CP powder into the 2% MFC hydrogel with a mass ratio of 1: 49: 14 corresponding to the dry matter of MFC: LS: CP, respectively. A commercial planetary blender (RP10, Proline) was used to homogenize the tri-component hydrogel.

2.2 Rheological tests

Rheological tests were conducted in two modes: simple shear mode for viscosity measurements and thixotropic mode for thixotropic tests. Regardless of modes, all rheological measurements were performed by using a rotational physical MCR 301 rheometer (Anton Paar) in a plate-cone configuration. A cone with 50 mm diameter and 1° angle was used and the gap was set to 1 mm. A transparent cover was used to prevent water evaporation during measurements. Temperature of the plate was maintained at 23 °C.

Viscosity measurements were carried out for all suspensions by repeating several cycles with shear rate ranging between 10^{-3} and 10^{3} s^{-1} with about 10 min relaxing time between each cycle. Four measuring points were set for decay with 10 s between each measuring point. Thixotropic measurements were carried out by maintaining the shear rate at 1000 s^{-1} for 20 s before a sudden drop to 0.1 s^{-1}. Samples' viscosity and stress responses were recorded as a function of time.

2.3 Elaboration of carbon precursors by 3D printing and subsequent air drying

MFC/LS/CP carbon precursors were elaborated using a fused deposition modeling (FDM) 3D printer (Leapfrog, Creatr HS model) equipped with a screw-pump paste extruder (Wasp, claystruder). The tri-component slurry was stored in a syringe with the plunger being pushed under a steady pressure (about 1 bar) and it passed through a dispensing screw-pump before being printed via a 0.5 mm needle. The printing speed, the width of filament as well as the layer height were set to 550 mm/min, 0.6 mm and 0.33 mm, respectively, in order to attain a good printing definition at a relatively high printing speed. Samples printed in various forms and patterns (such as cylinder, disc and web) were then air-dried at ambient temperature.

Only monolines of MFC/LS/CP mixture were printed using a 1mm needle for bending test purpose. They were then air-dried in ambient temperature.

2.4 Pyrolysis and thermal characterization by TGA/DTG

Pyrolysis of printed and then dried composites was conducted in a tubular oven (Carbolite®, type 3216) under nitrogen flux. The heating program is shown in Table 1, with reference to Kercher at *al.* [20]. Chars at the exit of oven were washed by HCl solution to eliminate the mineral matters water by following the protocol of Takagi et al. [32].

The thermal stability of MFC/LS/CP composites was examined by thermogravimetric analysis (TGA) in a thermobalance (STA6000, Perkin Elmer) under nitrogen atmosphere. The temperature program has been detailed in an earlier work [26].

Table 1 Heat treatment program.

T range (°C)	Heating rate (°C/min)	Dwell time at final temperature (min)
Ambient~150	0.5	60
150~400	0.2	-
400~600	0.5	-
600~target T (600~1000)	1	10

2.5 Characterization of the resulting carbons

2.5.1 Microscopy

Morphological characterization was performed on the surface and sections of disc-like samples (except for CP) using a scanning electron microscope (FEI-Quanta 2000, ESEM^{TM}).

2.5.2 Electrical conductivity measurements

Electrical measurements were performed on carbons in the form of disc using a four-point probe system (Standa 019759) by following ASTM C611-98 (2005) and ASTM F84-98.

The current was generated by an impendence analyzer (Jandel, model RM3). The thickness of samples was measured by a Vernier caliper. A correction factor was used to compensate the small dimensions of each sample according to the work of Smits et al. [33]. 5 disk-like samples were measured for each HTT (heat treatment temperature).

2.5.3 Density measurements

Bulk densities (geometric densities) were obtained by weighting and geometric measurements (disc samples). A Vernier caliper was used for geometric measurements. Skeletal density (true density) was measured using a gas displacement pycnometry system (AccuPyc 1330, Micromeritics, USA). Helium was used as displacement gas thanks to its extreme inertness (avoid being adsorbed) and the small molecule size (about 0.2 nm) [34], thus it can penetrate even the micropores in the sample. Before skeletal density measurement, samples were grounded in order to minimize the effect of closed porosity.

2.5.4 Microstructural characterization

Microstructure characterization (Raman and X-ray diffraction) was conducted only for 1000°C-carbonized MFC/LS/CP carbon. Raman spectra were recorded using a Renishaw in-via Raman micro-spectrometer. A 100 mw, 785 nm laser was passed through a 1% transmission filter before projecting a measurement spot on samples with a diameter of approximately 1.5 µm. A 50x objective was used and frequencies between 800 and 2000 cm^{-1} were scanned in a synchroscan mode for each spectrum. 10 spectra were collected for each char sample representing 10 different measured positions. The average of 10 spectra was calculated to represent the Raman pattern of one sample. The spectrum of each sample was then smoothed and normalized to its own G-band position (around 1600 cm^{-1}). As presented in **Erreur ! Source du renvoi introuvable.**, 5 Gaussian peaks (at around 1200, 1330, 1500,

1585, 1750 cm^{-1}, respectively) were assigned based on data from previous work [35]-[40] by considering the shape of the spectra and for the sake of highlighting the characteristic bands.

X-ray diffraction (XRD) was used for phase and crystal structure identification. Each char, in the form of plate thin film, was placed on the sample holder and levelled to obtain total and uniform X-ray exposure. The samples were analyzed using an X-ray diffractometer (X'pert Pro MPD, PANalytical) at room temperature (RT) with a monochromatic CuKα radiation source (λ = 0.154 nm) in the step-scan mode with a 2θ angle ranging from 5° to 70° by a step of 0.067° and scanning time of 6.0 min.

Diffractograms of all samples were smoothed, normalized to 2θ =70° and linear-subtracted as described in [10]. Average crystallite size, along c- and a- axis was determined using Scherrer equations [20][32][41] (Eq 1 &Eq 2):

Eq 1 $$L_c = 0.89\lambda/B_c cos\theta_c$$

Eq 2 $$L_a = 1.84\lambda/B_a cos\theta_a$$

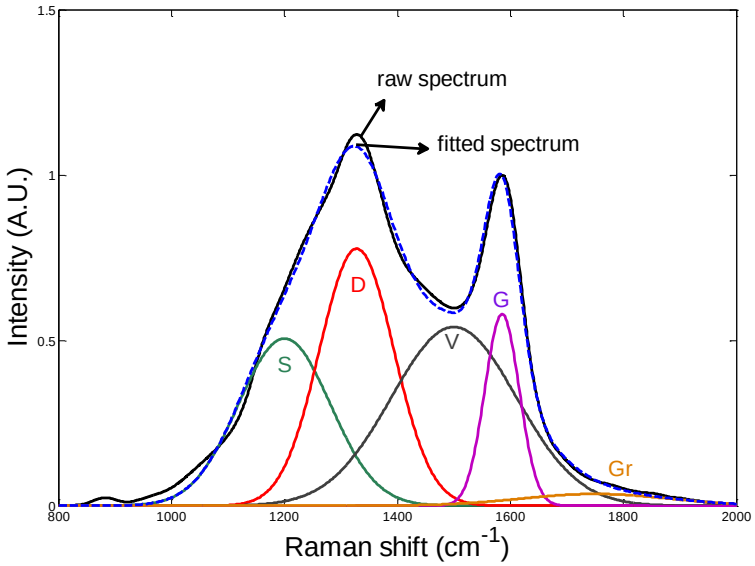

Fig 1 Assignment of Raman bands. The D band (1320 cm^{-1}) is due to sp^2 bonds in highly ordered carbonaceous materials (aromatic rings with not less than 6 rings), the G band (1580 cm^{-1}) to sp^2 bonds in graphitic carbons, the S, V and Gr bands (at 1180, 1465 and 1800 cm^{-1}) to sp^2 and sp^3 bonds in amorphous carbons with small aromatic rings [38].

Where L_c, and L_a are the stacking height and the lateral size of the crystallite, respectively; λ is the wavelength of the used X-ray; B_c and B_a are respectively the full width half maximum (FWHM) of the (002) and (100) peaks from the diffractogram of each sample, whereas θ_c and θ_a are the corresponding scattering angles.

The interlayer spacing d_{002} was determined using Bragg's law: Eq 3

Eq 3 $$d_{002} = \lambda/2sin\theta_c$$

The number of crystallite layers per stack (N) was therefore calculated as: Eq 4

Eq 4 $$N = L_c/d_{002} + 1$$

2.5.5 Mechanical characterization by 3-point bending tests

A dynamic mechanical analyzer DMA (TA RSA3) equipped with a three-point bending fixture (Lxlxh:10x12.5x19 mm) was used for mechanical characterization of MFC/LS/CP carbon precursor and the resulting carbons. The tested samples were 3D printed mono-lines that were (or not) subsequently carbonized at HTT from 400 to 1200°C. The standard of ISO 178 was followed except for the special dimensions of the samples. The cross section of each samples is approximately an ellipse, as a result, the corresponding section modulus was used to calculate the flexural stress and strain as well as elastic modulus. The crosshead speed was set to 0.001 mm/s in order to obtain enough data before rupture. 3 samples were tested for each HTT in order to examine the inhomogeneity of the samples. For each sample, 6 different positions were measured in major and minor axis by a Vernier caliper for the estimation of the uncertainty caused by dimension measurement. The average value and the standard deviation of elastic modulus or peak stress were thus calculated from the 18 values.

3. Results and discussion

3.1 Rheological properties of MFC/LS/CP hydrogel

The improvement of rheological properties by the addition of CP is shown in **Erreur ! Source du renvoi introuvable.**. The viscosity still keeps the shear-thinning profile but is strengthened by 2-3 magnitudes due to 22% of CP (weight fraction, $W_{cp}/(W_{cp}+W_{water})$) added into the pristine MFC/LS hydrogel. More importantly, the time for network restauration is largely shortened, from 27 s to 4 s (since MFC/LS/CP is quite similar to pure MFC behavior)[15], with the presence of CP. The printing results (**Erreur ! Source du renvoi introuvable.**a)) confirmed the usability of as-formulated hydrogel.

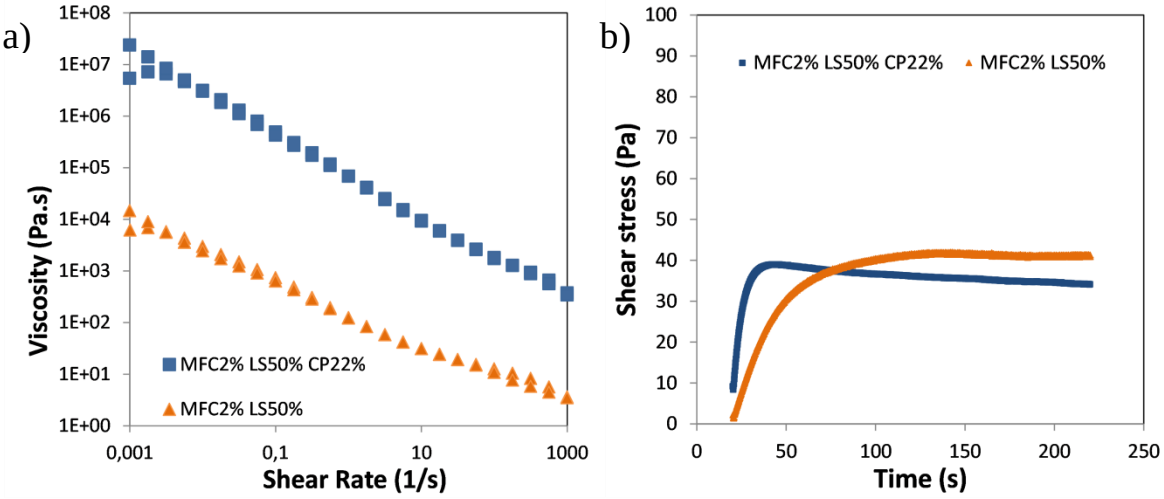

Fig 2 Rheograms a) and b) shear stress variation after a step down shear rate drop from 1000 to 0.1 s^{-1} (high shear rate data, t < 20 s, are not plotted since higher than 100 Pa) of the MFC/LS/CP hydrogel, compared to the corresponding binary one (MFC/LS).

3.2 Macro- and micro-morphology of MFC/LS/CP precursor and the resulting carbons

The photographs of 3D-printed MFC/LS/CP precursor composites are displayed in **Erreur ! Source du renvoi introuvable.**a). After air-drying in ambient temperature, the dry objects still maintain their original shape and definition without visible defects due to the evaporation of water. Carbons derived from their corresponding precursor are surprisingly well-shaped and also without major surface and sectional irregularities although a rather important shrinkage occurred during the pyrolysis (**Erreur ! Source du renvoi introuvable.**b). As a

result, the excellent morphological stability of the MFC/LS/CP carbon precursor could be concluded, that is the cornerstone of further characterizations of as-elaborated carbons.

The micro-scaled morphology of the samples is presented in **Erreur ! Source du renvoi introuvable.** using a SEM. The used cellulose powder (CP) particles (**Erreur ! Source du renvoi introuvable.**a) have an average length of 50µm and look like pieces cut from the much longer cotton linters. Its presence in the MFC/LS/CP composite can be clearly seen from the surface of the latter (**Erreur ! Source du renvoi introuvable.**.b). Such composite has a typically "almond chocolate" construction in which CP is more like the tiny pieces of almond wrapped by the "chocolate" surrounding that is made of MFC/LS. Since MFC was included in the composite in very small quantity and also because of its tiny dimension, it is less visualized than LS in the "chocolate-like" MFC/LS background. Furthermore, pyrolysis leads to limited changes on the sample surface except largely broadening and intensifying the fissures among which some seem already existed after drying (**Erreur ! Source du renvoi introuvable.**b & c). Besides, it "smooths" the surface due to the low residue of CP at 1000°C (confirmed by **Erreur ! Source du renvoi introuvable.**c). However, images of samples' section (**Erreur ! Source du renvoi introuvable.**d & e) reveal an important appearance of macro-pores that is very likely to be the result of CP decomposition during pyrolysis by accounting the dimensions of pores (multi-diameters, up to 50 µm) as well as the fact that CP was wrapped randomly in three-dimension by the MFC/LS surrounding. The significant improvement of the porosity by the addition of CP in the formulation will lead to a more promising use of the studied bio-carbons in energy storage devices. In addition to that, it is worth noticing that although the sample was constructed with printed filaments(diameter = 500 µm), no single filament was identified from the section image in micro-scale (**Erreur ! Source du renvoi introuvable.**d), signifying that all filament were molten together after deposition and the samples is rather homogeneous in terms of the distribution of the matter.

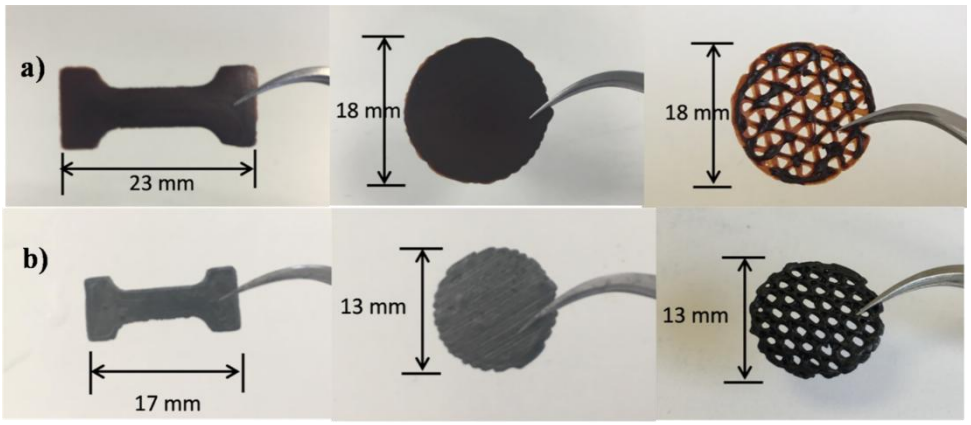

Fig 3 Photographs of: a) 3D-printed objects from MFC/LS/CP hydrogel after air-drying and b) after pyrolysis at 1000°C

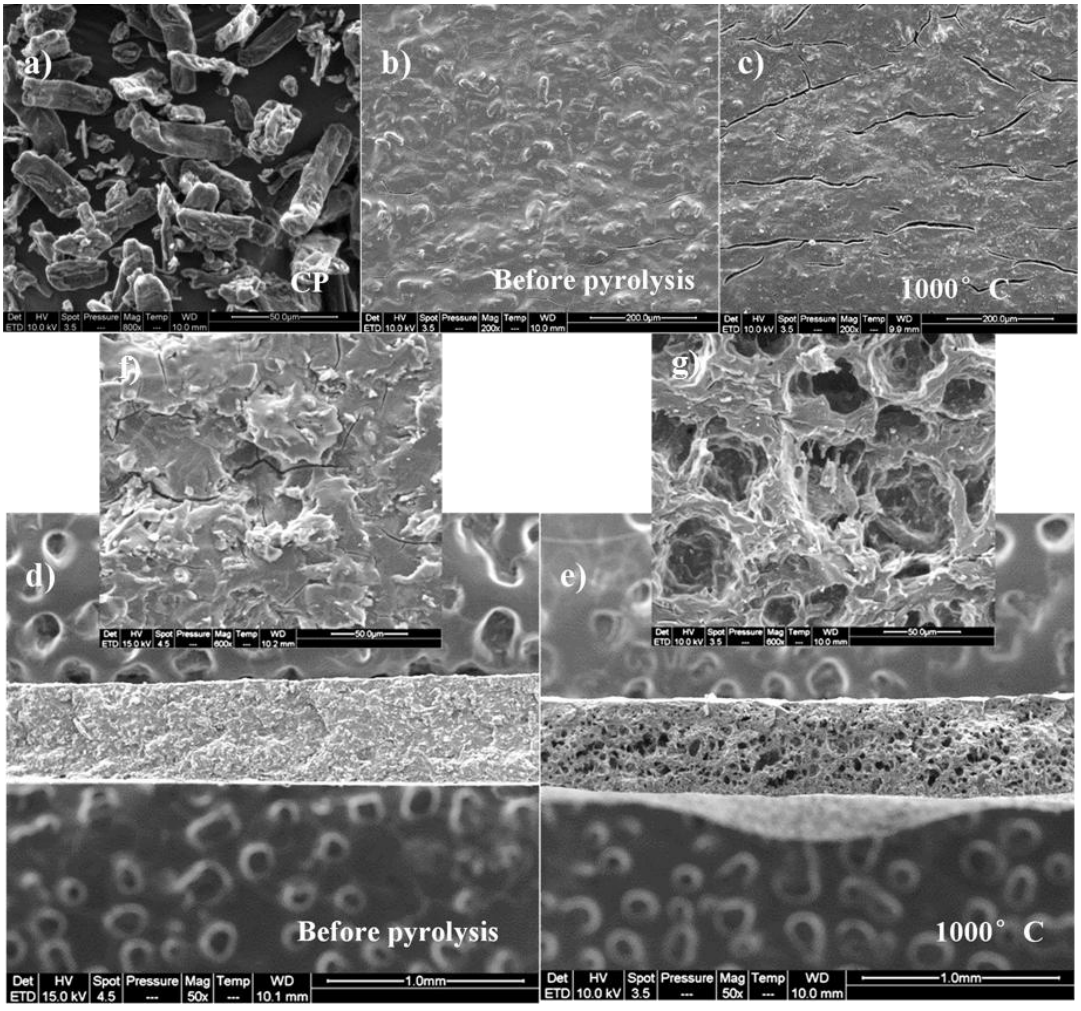

Fig 4 SEM observation of: a) as-received cellulose powder (CP); b) and c) surface of MFC/LS/CP precursor composite and its carbon after pyrolysis at 1000°C, respectively; d) and e) transversal section of samples corresponding to b) and c), respectively; f) and g) a zoomed part of d) and e), respectively.

3.3 Analysis of pyrolytic process of MFC/LS/CP composite

The TGA and DTG patterns of the tri-component composite are presented in **Erreur ! Source du renvoi introuvable.**a and b and are compared to those of its constituents: cellulose powder and the binary composite of MFC/LS. CP exhibits a typical cellulose degradation peak at around 325°C with the maximum reaction rate reaching 13.2%/min (or 2.64%/°C). Its thermal degradation profile shows no difference compared to the published one in [32] where CP of the same origin (Aldrich, 50 µm) was examined. One remarkable phenomenon is that the used cellulose powder (powder form) decomposes much more intensively than microfibrillated cellulose (in the form of a fibrillated web), 13.2%/min compared to 6.1%/min and reaches the maximum reaction rate at a slightly lower temperature (325°C with regard to 334°C, respectively), as shown in **Erreur ! Source du renvoi introuvable.**c). MFC is composed of smaller cellulose fibrils (L ≈ 10 µm, D ≈ 2-50 nm [22]) than CP. Due to the huge quantity of inter-fibril hydrogen bonds that construct the MFC "web", MFC decomposition is more or less inhibited [43]-[45]. As a result, MFC is thermally more stable than the powder formed CP. However, in the range of 230°C-300°C, MFC degrades slightly stronger than CP, probably due to its hemicellulose component [46] whose decomposition normally occurs at this temperature [47]. In addition to that, many other factors may also affect thermal degradation of cellulosic products, such as cellulose source [48], bleaching degree [49], crystallinity [50] and impurities [51].

Furthermore, it is remarkable that the triplet is rather thermally stable by generally following the thermal profile of its most important constituent, the binary composite, except for the region between 200°C and 280°C. Throughout this temperature range, the reaction rate of the triplet is slightly higher than the binary composite, possibly due to the proportion of CP whose decomposition was catalyzed by the presence of Na from the binary composite by shifting to lower temperatures, as was proved in an earlier study [26]. The temperature shift of

CP could be quantified from **Erreur ! Source du renvoi introuvable.**a where the theoretically calculated curve assuming an additivity law is obtained using Fig 6 a) experimental and calculated DTG curves of the ternary composite MFC/LS/CP; b) effect of the sodium content on the drop (ΔTp) of the maximum reaction rate temperature (the point representing the triple composite is indicated by a flash whereas the others represent MFC/LS composites

Eq 5. The sodium-induced temperature shift of cellulose powder is consistent with the previously determined linear relationship describing how sodium content influences MFC decomposition in MFC/LS composites, as shown in **Erreur ! Source du renvoi introuvable.**b.

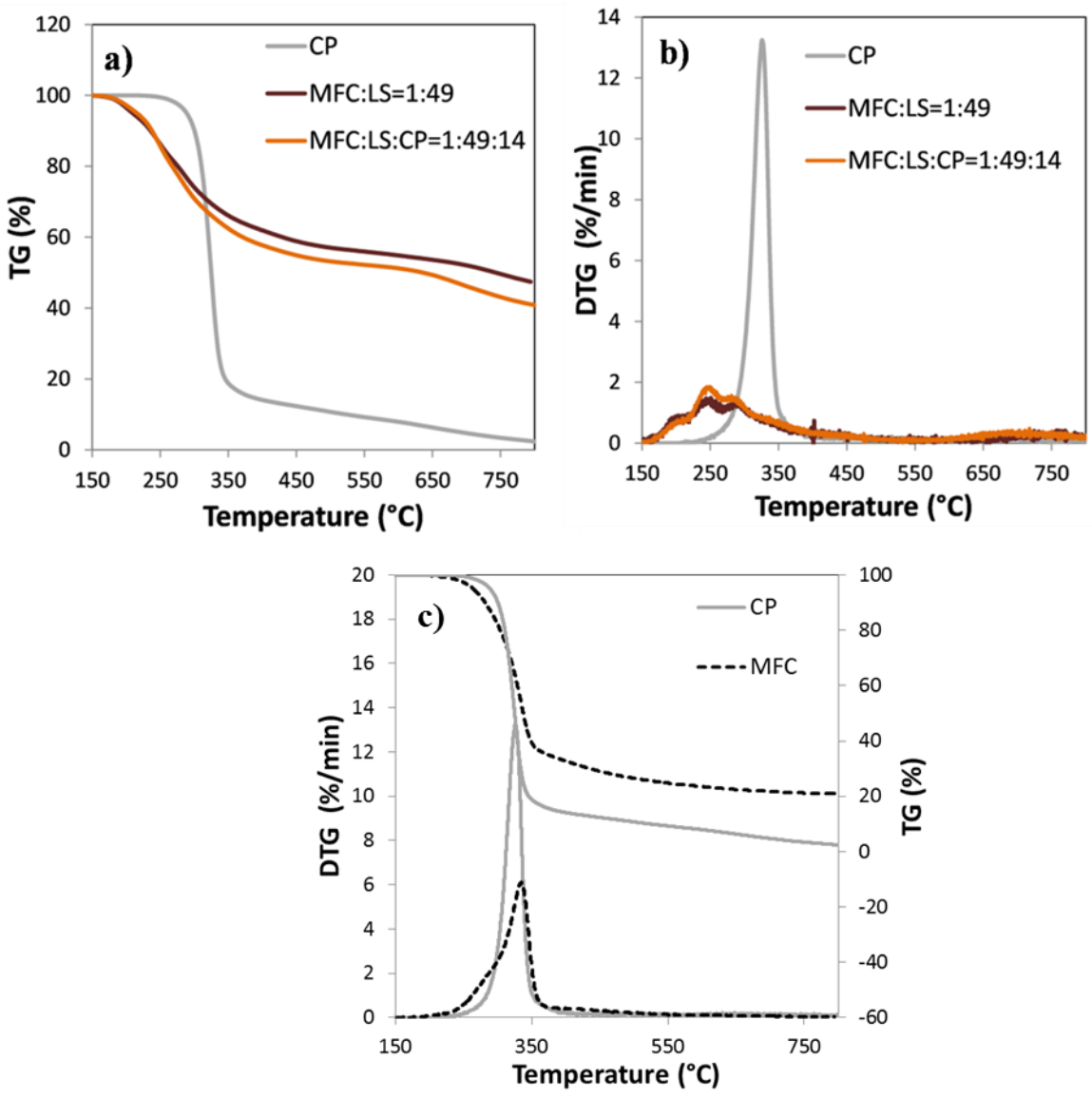

Fig 5 TG a) and DTG b) curves of the MFC/LS/CP composite and its constituents (cellulose powder and the composite MFC/LS); c) a comparison of thermal degradation between CP and MFC

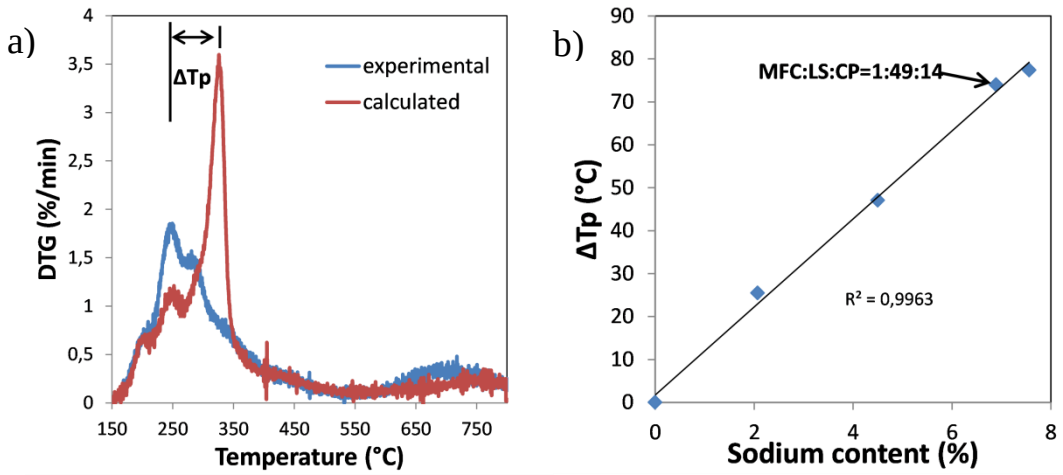

Fig 6 a) experimental and calculated DTG curves of the ternary composite MFC/LS/CP; b) effect of the sodium content on the drop (ΔTp) of the maximum reaction rate temperature (the point representing the triple composite is indicated by a flash whereas the others represent MFC/LS composites

Eq 5 $$DTG(T)_{calculated} = \%\,CP \times DTG(T)_{CP} + \%binary\ composite \times DTG(T)_{binary\ composite}$$

3.4 Characterization of MFC/LS/CP carbons

3.4.1 Density evolution

Erreur ! Source du renvoi introuvable. exhibits both bulk and skeletal (true) densities of printed MFC/LS/CP "disk" and those of its derived carbons. According to it, the skeletal density of MFC/LS/CP carbon precursor is only slightly higher than the bulk one, 1.53 compared to 1.31 g/cm^3. It should be attributed to the low porosity that exists in such composite, *ca.* 0.146, induced by air-drying (as shown in **Erreur ! Source du renvoi introuvable.**. During pyrolysis when HTT increases from 400 to 1200°C, quite different evolutions are observed for skeletal and bulk density. Skeletal density of the obtained carbons globally rises from 1.43 to 1.84 g/cm^3 for a HTT increase from 400 to 1200°C, except for 900 and 1000°C, for which a slight density drop is observed. As commonly reported in the

literature [52]-[55], such an increase of skeletal density with HTTs is considered as reflecting the continuous synthesis of highly organized carbon structures (tuborstratic structures) that are more compact and denser than disordered carbon [52],[53].

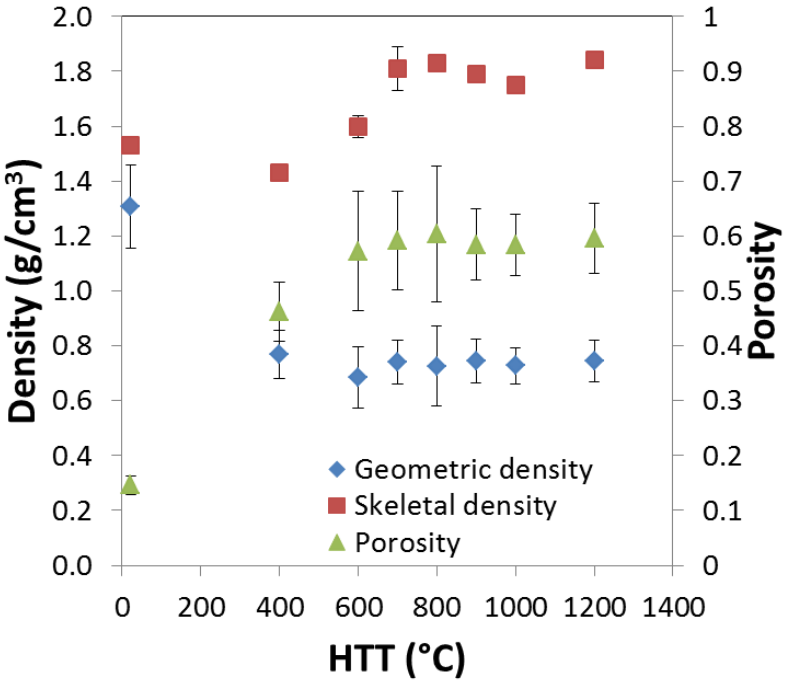

Fig 7 Density and porosity evolution of MFC/LS/CP carbons as a function of the heat treatment temperature. Error bars represent data standard deviation.

During pyrolysis, non-conjugated molecules either decompose as volatiles or convert into conjugated ones and the chars undergo aromatic condensation. Due to the existence of defects (oxygen components that are heat-resistant) and the randomly oriented graphite crystals (turbostratic nature), the maximum skeletal density of biochars is always below that of graphite (2.25 g/cm^3) [52],[55].

Bulk density of biocarbons is the result of the competition between the HTT-induced weight loss and volumetric shrinkage. Bulk density importantly drops from 1.31 to 0.77 g/cm^3 when HTT increased at 400°C. After 400°C, the bulk densities of MFC/LS/CP carbons fluctuate within the range of 0.68 and 0.73 g/cm^3, which seems to be less HTT-influenced.

The calculated porosities also increases with HTTs (**Erreur ! Source du renvoi introuvable.**) at early stage of pyrolysis before stabilizing after 600°C, which is in agreement with the previous SEM observation (**Erreur ! Source du renvoi introuvable.**) and the literature [53][54]. Compared to MFC/LS carbons (not shown here), those derived from MFC/LS/CP precursor have significantly higher porosities, *ca.* 0.6 with regard to 0.37 at 1200°C. This value is approaching the result that was reported for wood chars [52]. The distinguished porosity between MFC/LS and MFC/LS/CP carbons is associated with the presence of CP in the formulation of the latter. According to its thermal degradation pattern in **Erreur ! Source du renvoi introuvable.**c as well as the SEM observation in **Erreur ! Source du renvoi introuvable.**e, CP nearly disappears after 600°C (carbon yield <5%) thus leading to the formation of the pores whose dimensions are visibly similar to those of CP particles. Thereby, a controlled porosity in the resulting carbons could be expected by simply a good dosage of CP quantity in the formulation of carbon precursor.

3.4.2 Microstructural evolution

The mutual evolution of the 3 identified phases (defect-free and defected graphene stacks as well as amorphous structures) [18] in the as-elaborated carbons provides essential information to understand the changes of their electrical and mechanical properties. Raman and X-ray analysis revealed that the structures of MFC/LS based carbons get ordered with the increasing temperatures (Raman band of D and G, as well as crystal size L_a increase with HTTs). These results have been detailed in a submitted paper focusing on the development of the electrical conductivity of these MFC/LS based carbons and its relationship with the micro-structure.

For these 3D printed carbons, microstructure analysis was conducted only for 1000°C-carbonized MFC/LS/CP carbon with comparison to MFC/LS carbon under same synthesis conditions. As shown in **Erreur ! Source du renvoi introuvable.** and Fig 8 a) Raman spectrum

and b) XRD diffractogram of 1000°C-synthesed MFC/LS/CP carbon, compared to the corresponding MFC/LS carbon.

Table 2, both carbons present similar profiles in Raman spectra and XRD diffractograms, owing to their same fundamental constituents. Nevertheless, the small difference in proportions between LS-based precursor and cellulose-based precursors (MFC and CP) as well as their different aromatic condensation mechanisms during pyrolysis still led to a slight distinction in microstructural parameters as shown in Fig 8 a) Raman spectrum and b) XRD diffractogram of 1000°C-synthesed MFC/LS/CP carbon, compared to the corresponding MFC/LS carbon.

Table 2.

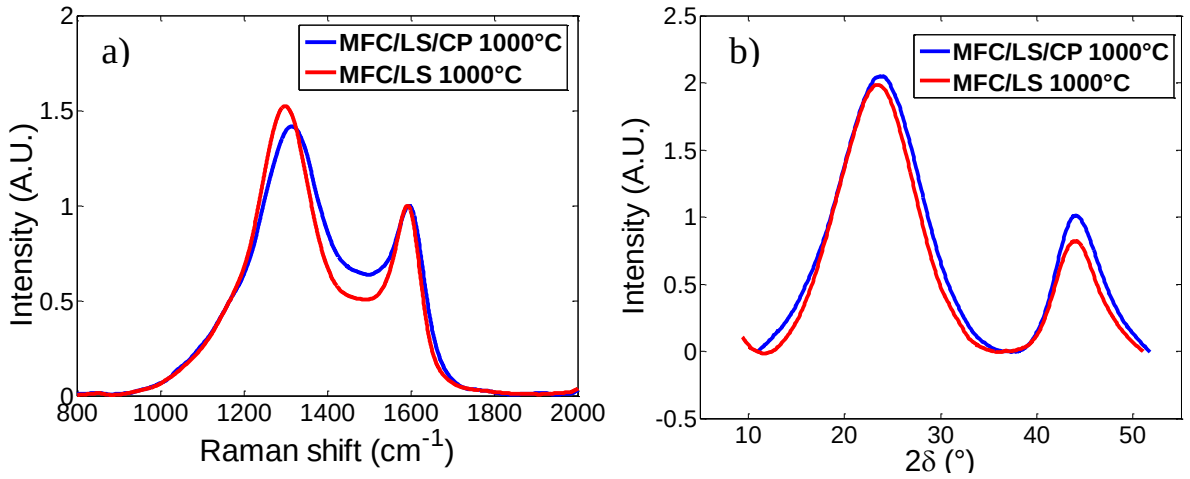

Fig 8 a) Raman spectrum and b) XRD diffractogram of 1000°C-synthesed MFC/LS/CP carbon, compared to the corresponding MFC/LS carbon.

Table 2 Structural parameters MFC/LS/CP and MFC/LS carbons obtained at 1000°C calculated using Raman and XRD spectra and Eqs. 1-4.

Precursor	LS proportion (%)	d_{002} (nm)	L_c (nm)	L_a (nm)	N	Raman band I_{D+G}/I_{total}
MFC:LS:CP=1:49:14	76.6	0.37	0.81	3.22	3.2	0.4768
MFC:LS=1:5.25	84	0.38	0.86	3.39	3.2	0.5047

At 1000°C, MFC/LS/CP carbon contains less LS, 76.6% compared to 84% in MFC/LS carbon, which resulted the smaller size of graphene stacks and higher content of ordered structures (D+G ratio) although to a very limited degree.

3.4.3 Electrical conductivity

The bulk and the calculated skeletal conductivities (using Fig 9 Bulk and skeletal electrical conductivity of MFC/LS/CP carbons plotted as a function of the heat treatment temperature (HTTs). The conductivity of MFC/LS carbon obtained at 1000°C is given for comparison.

Carbon skeletal conductivity was calculated according to an open foam model [57]:

Eq 6 [19][20][56]) of MFC/LS/CP carbons are displayed in

. According to it, both skeletal and bulk conductivity of MFC/LS/CP carbons are highly HTT-depended and present 3 different regions [18][19]: i) the appearance of mutual contacts between conductive carbon clusters when 600°C ≤ HTT ≤ 700°C for which the skeletal electrical conductivity underdoes a sharp rise of 3 orders of magnitude, *ca.* from 0.001 to 1.054 S/cm; ii) the steady intensification of such contacts which arises from the growth of the conductive clusters for 700≤HTT≤1000, leading to a continuous improvement of the electrical conductivity from 1.1 to 164.6 S/cm ; iii) the slowed-down increase of the conductivity due to the already established current pathways that will be less-influence by the growth of conductive clusters for HTT>1000°C. Moreover, the difference between the bulk and skeletal density that increases at elevated HTT confirms the fact that the resulting carbons possess a more and more important porosity during pyrolysis, as revealed by density measurement (**Erreur ! Source du renvoi introuvable.**). At 1000°C, MFC/LS carbon has a slightly higher skeletal conductivity than MFC/LS/CP carbon, 173.5 S/cm with regard to 164.6 S/cm. Such a difference collaborates with the previous observations in Fig 8 a) Raman spectrum and b) XRD diffractogram of 1000°C-synthesed MFC/LS/CP carbon, compared to the corresponding MFC/LS carbon.

Table 2 that MFC/LS owns slightly larger size of graphene stacks and higher structural ordering (represented by D+G band ratio), that have been proved to be positively correlated with the electrical conductivity that is developed in engineering carbons during pyrolysis [40].

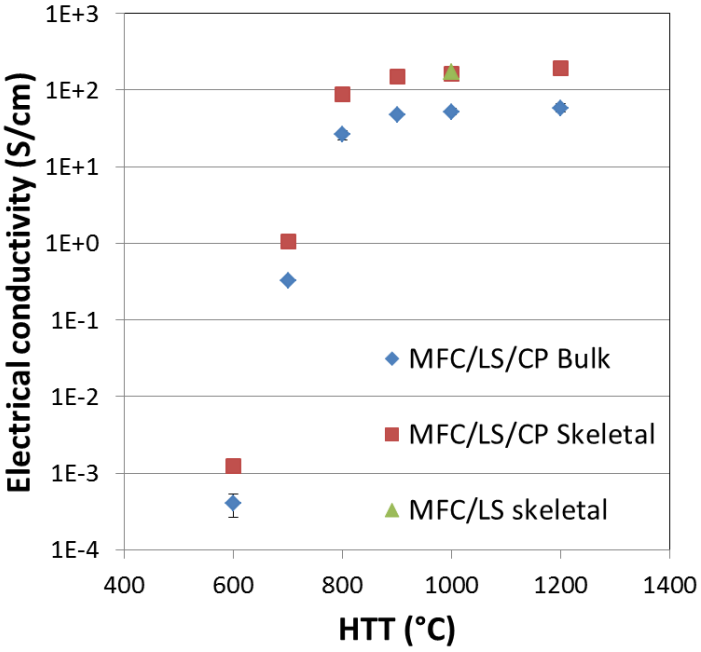

Fig 9 Bulk and skeletal electrical conductivity of MFC/LS/CP carbons plotted as a function of the heat treatment temperature (HTTs). The conductivity of MFC/LS carbon obtained at 1000°C is given for comparison.

Carbon skeletal conductivity was calculated according to an open foam model [57]:

Eq 6 $$\sigma/\sigma_s = \frac{1}{3}(\rho/\rho_s) + \frac{2}{3}(\rho/\rho_s)^{1.5}$$

Where σ and σ_s are the bilk and skeletal conductivities and ρ and ρ_s are the bulk and the skeletal densities.

3.4.4 Mechanical properties

Pyrolysis-induced modifications of the mechanical strength of MFC/LS/CP samples were characterized by 3-point bending test. Despite the occasionally important deviation which is caused by the commonly reported heterogeneity [30][58][59] of engineering carbons (due to

disordered or turbostratic carbon structures), the results shown in **Erreur ! Source du renvoi introuvable.** display a strongly HTT-dependent mechanical behavior for as-produced carbons Whether carbonized or not, MFC/LS/CP are elasticity-dominated materials with no plastic zone except for non-carbonized ones for which a short plastic zone just before rupture was observed. The slope, known as elastic modulus E_f, and the peak stress from each stress-strain curve are exhibited as function of HTTs in **Erreur ! Source du renvoi introuvable.**a and b. MFC/LS/CP carbon precursor exhibits a flexural elastic modulus of 4.05 GPa and a peak stress of 23.5 Mpa, according to **Erreur ! Source du renvoi introuvable.**. Compared to the precursor, the carbonaceous char obtained at 400°C lose much mechanical strength reflecting in both elastic modulus and peak stress. It is associated with the intensive mass loss due to devolatilization that the char suffers from during this temperature range. The diminished mechanical property also coincides with the decrease of the skeletal and bulk density of MFC/LS/CP at 400°C (**Erreur ! Source du renvoi introuvable.**). When HTT increases to 600-900°C, the temperature-strengthened mechanical properties become visible. Both flexural modulus and peak stress rise quite linearly with HTTs and reach their maximum (6.6 GPA and 29.8 MPa, respectively) at 900°C. After 900°C, further carbonization is found to lower the mechanical strength of the carbons.

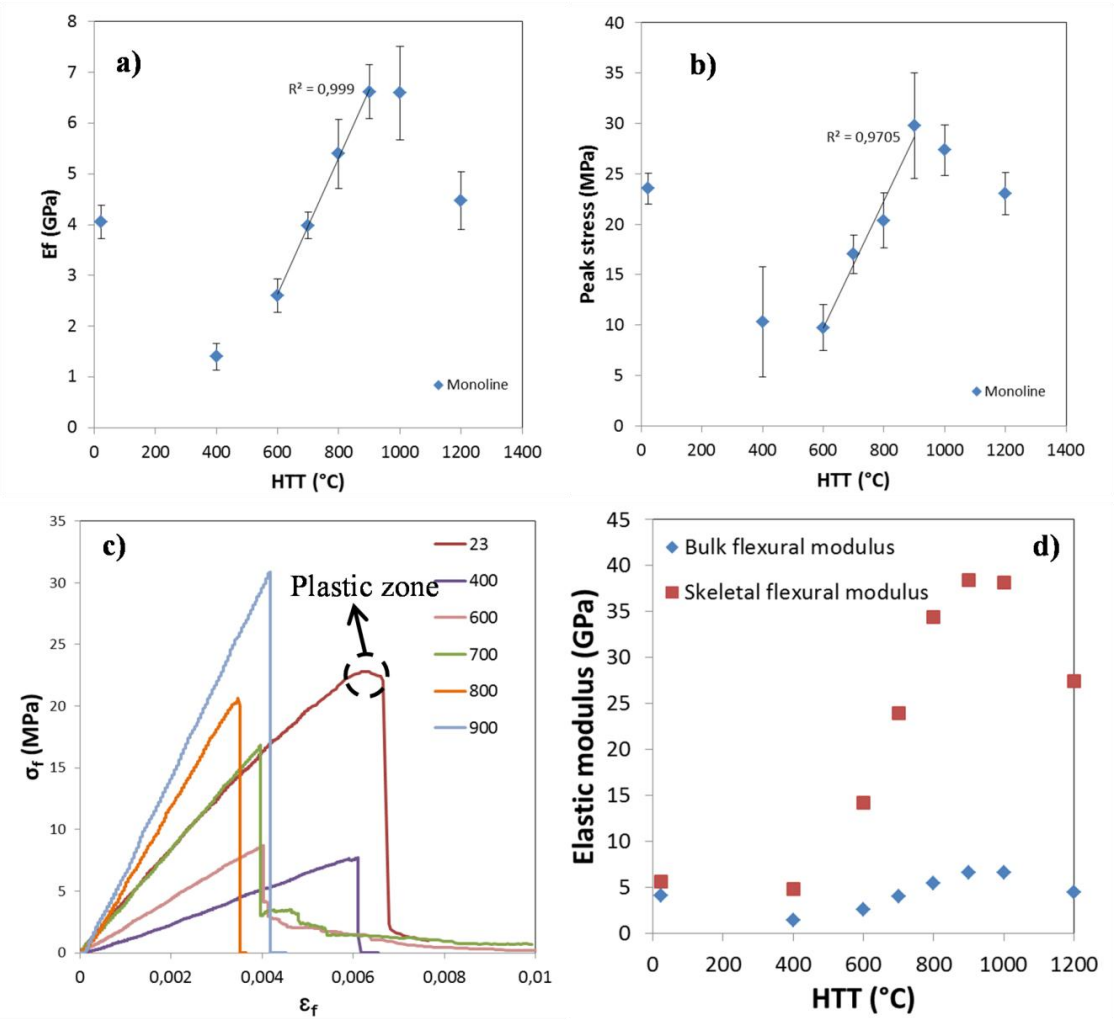

Fig 10 a) Elastic modulus and b) peak stress of MFC/LS/CP monolines pyrolyzed at different HTTs from 3-point bending tests; c) the flexural stress-strain profile of the samples; d) calculated skeletal elastic modulus with comparison to bulk ones. Error bars represent data standard deviation.

A linear-elastic beam deflection model was used to approximate the flexural modulus of the hard carbon of MFC/LS/CP [20]**Erreur ! Source du renvoi introuvable.**, as shown in Eq 7:

Eq 7 $$E/E_s = (\rho/\rho_s)^2$$

Where E and E_s correspond to the bulk and skeletal elastic modulus of the carbon; ρ and ρ_s are respectively the bulk and skeletal density. The approximate Young's modulus data of the MFC/LS/CP hard carbon are displayed in **Erreur ! Source du renvoi introuvable.**d. Because of the porosity effect, the skeletal modulus is found to be higher than the bulk one and the difference between them is largely pronounced throughout the HTT range of 600-1200°C

where the porosity is also intensively present. The resulting hard carbon achieves the best Young's modulus as high as 38.4 GPa at 900°C, that is nearly 1.5 higher than that of polycrystalline graphite (27 GPa [20]**Erreur ! Source du renvoi introuvable.**).

4 Conclusion

The current study examined the feasibility of manufacturing electrically conductive and mechanically resistant carbon structures by 3D printing and subsequent pyrolysis using MFC/LS/CP formulation. MFC, LS and CP are purely bio-sourced materials. Their water-processing and interesting rheological properties (high viscosity, shear-thinning profile and the short relaxation time) account for the success of manufacturing well-shaped hydrogels by 3D printing in the present work. The printed MFC/LS/CP hydrogels were proved to be morphologically stable to air drying and to the subsequent pyrolysis. Owing to the presence of CP that is thermally less-stable, the resulting carbons exhibit improved porosity at elevated HTTs, compared to MFC/LS carbons. Such an increase in porosity and in the material specific surface area is supposed to promote the use of MFC/LS/CP carbons in energy storage devices owing to an increased interfacial area between the charge carrier (electrolyte) and the carbon-based electrode. At 900°C, MFC/LS/CP carbons not only result in a high electrical conductivity of 47.8 S/cm coupled to a low bulk density of 0.74 g/cm^3 (corresponding to a porosity of 0.58), but also achieve an elastic modulus of 6.6 Gpa. It is believed by authors that the interesting electrical and mechanical results obtained will lead to a promising application as electrode materials for MFC/LS/CP biocarbons in close future.

Acknowledgments

This work was supported by Grenoble-INP and Grenoble Alpes University (Grant AGIR) and the PolyNat Carnot Institute (Investissements d'Avenir-Grant Agreement N° ANR-16-CARN-0025-01). LGP2 is part of LabEx Tec21 (Investissements d'Avenir, Grant Agreement

ANR-11-LABX-0030). The authors would like to acknowledge Pr. Sylvain SALVADOR, from the Center RAPSODEE- Ecole des Mines-Albi, for his help in the measurement of the skeletal densities of carbons.

References

[1] T. D. Ngo, A. Kashani, G. Imbalzano, K. TQ. Nguyen, D. Hui, Additive manufacturing (3D printing): A review of materials, methods, applications and challenges, Compos. Part B 143 (2018) 172–196.

[2] X. Wang, M. Jiang, Z. Zhou, J. Gou, D. Hui, 3D printing of polymer matrix composites: A review and prospective, Compos. Part B 110 (2017) 442-458.

[3] L. C. Hwaa, S. Rajoo, A. Mohd Noor, N. Ahmad, M.B. Uday, Recent advances in 3D printing of porous ceramics: A review, Curr. Opin. Solid State Mater. Sci 21 (2017) 323–347.

[4] X. Tian, T. Liu, C. Yang, Q. Wang, D. Li, Interface and performance of 3D printed continuous carbon fiber reinforced PLA composites, Compos. Part A 88 (2016) 198–205.

[5] R. T. Luiz Ferreira, I. C. Amatte, T. Assis Dutra, D. Bürger, Experimental characterization and micrography of 3D printed PLA and PLA reinforced with short carbon fibers, Compos. Part B 124 (2017) 88-100.

[6] G. Postiglione, G. Natale, G. Griffini, M. Levi, S. Turri, Conductive 3D microstructures by direct 3D printing of polymer/carbon nanotube nanocomposites via liquid deposition modeling, Compos. Part A 76 (2015) 110–114.

[7] K. Gnanasekaran, T. Heijmans, S. van Bennekom, H. Woldhuis, S. Wijnia, G. de With, H. Friedrich, 3D printing of CNT- and graphene-based conductive polymer nanocomposites by fused deposition modeling, Appl. Mater. Today 9 (2017) 21–28.

[8] D. Zhang, B. Chi, B. Li, Z. Gao, Y. Du, J. Guo, J. Wei, Fabrication of highly conductive graphene flexible circuits by 3D printing, Synth. Metals 217 (2016) 79–86.

[9] D. Espalin, D. W. Muse, E. MacDonald, R. B. Wicker, 3D Printing multifunctionality: structures with electronics, Int. J. Adv. Manuf. Technol. 72 (2014) 963–978.

[10] J. A. Lewis, Direct Ink Writing of 3D Functional Materials, Adv. Funct. Mater. 16 (2006) 2193-2204.

[11] L. Jabbour, R. Bongiovanni, D. Chaussy, C. Gerbaldi, D. Beneventi, Cellulose-based Li-ion batteries: a review, Cellulose. 20 (2013) 1523–1545. doi:10.1007/s10570-013-9973-8.

[12] L. Zolin, M. Destro, D. Chaussy, N. Penazzi, C. Gerbaldi, D. Beneventi, Aqueous processing of paper separators by filtration dewatering: towards Li-ion paper batteries, J. Mater. Chem. A. 3 (2015) 14894–14901.

[13] G. Nyström, A. Marais, E. Karabulut, L. Wågberg, Y. Cui, M.M. Hamedi, Self-assembled three-dimensional and compressible interdigitated thin-film supercapacitors and batteries, Nat. Commun. 6 (2015) 7259. doi:10.1038/ncomms8259.

[14] W.-J. Liu, K. Tian, Y.-R. He, H. Jiang, H.-Q. Yu, High-Yield Harvest of Nanofibers/Mesoporous Carbon Composite by Pyrolysis of Waste Biomass and Its Application for High Durability Electrochemical Energy Storage, Environ. Sci. Technol. 48 (2014) 13951–13959. doi:10.1021/es504184c.

[15] J. Jin, B. Yu, Z. Shi, C. Wang, C. Chong, Lignin-based electrospun carbon nanofibrous webs as free-standing and binder-free electrodes for sodium ion batteries, J. Power Sources. 272 (2014) 800–807. doi:10.1016/j.jpowsour.2014.08.119.

[16] Y. Wang, Y. Zou, J. Chen, G.-D. Li, Y. Xu, A flexible and monolithic nanocomposite aerogel of carbon nanofibers and crystalline titania: fabrication and applications, RSC Adv. 3 (2013) 24163. doi:10.1039/c3ra44820g.

[17] K.E. Perepelkin, Carbon fibres with specific physical and physicochemical properties based on hydrated cellulose and polyacrylonitrile precursors. A review, Fibre Chem. 34 (2002) 271–280.

[18] J.S. McDonald-Wharry, M. Manley-Harris, K.L. Pickering, Reviewing, Combining, and Updating the Models for the Nanostructure of Non-Graphitizing Carbons Produced from Oxygen-Containing Precursors, Energy Fuels. (2016). doi:10.1021/acs.energyfuels.6b00917.

[19] Y.-R. Rhim, D. Zhang, D.H. Fairbrother, K.A. Wepasnick, K.J. Livi, R.J. Bodnar, D.C. Nagle, Changes in electrical and microstructural properties of microcrystalline cellulose as function of carbonization temperature, Carbon. 48 (2010) 1012–1024. doi:10.1016/j.carbon.2009.11.020.

[20] A.K. Kercher, D.C. Nagle, Evaluation of carbonized medium-density fiberboard for electrical applications, Carbon. 40 (2002) 1321–1330. doi:10.1016/S0008-6223(01)00299-8.

[21] S.P. Mun, Z. Cai, J. Zhang, Fe-catalyzed thermal conversion of sodium lignosulfonate to graphene, Mater. Lett. 100 (2013) 180–183. doi:10.1016/j.matlet.2013.02.101.

[22] N. Lavoine, I. Desloges, A. Dufresne, J. Bras, Microfibrillated cellulose – Its barrier properties and applications in cellulosic materials: A review, Carbohydr. Polym. 90 (2012) 735–764. doi:10.1016/j.carbpol.2012.05.026.

[23] I. González, M. Alcalà, G. Chinga-Carrasco, F. Vilaseca, S. Boufi, P. Mutjé, From paper to nanopaper: evolution of mechanical and physical properties, Cellulose. 21 (2014) 2599–2609. doi:10.1007/s10570-014-0341-0.

[24] B.O. Myrvold, A new model for the structure of lignosulphonates: Part 1. Behaviour in dilute solutions, Ind. Crops Prod. 27 (2008) 214–219. doi:10.1016/j.indcrop.2007.07.010.

[25] Y. Shao, D. Chaussy, P. Grosseau, D. Beneventi, Use of Microfibrillated Cellulose/Lignosulfonate Blends as Carbon Precursors: Impact of Hydrogel Rheology on 3D Printing, Ind. Eng. Chem. Res. (2015). doi:10.1021/acs.iecr.5b02763.

[26] Y. Shao, C. Guizani, P. Grosseau, D. Chaussy, D. Beneventi, Thermal characterization and kinetic analysis of microfibrillated cellulose/lignosulfonate blends, J. Anal. Appl. Pyrolysis. 124 (2017) 25–34. doi:10.1016/j.jaap.2017.03.001.

[27] S.J. Haward, V. Sharma, C.P. Butts, G.H. McKinley, S.S. Rahatekar, Shear and Extensional Rheology of Cellulose/Ionic Liquid Solutions, Biomacromolecules. 13 (2012) 1688–1699. doi:10.1021/bm300407q.

[28] Y.-R. Rhim, D. Zhang, M. Rooney, D.C. Nagle, D.H. Fairbrother, C. Herman, D.G. Drewry III, Changes in the thermophysical properties of microcrystalline cellulose as function of carbonization temperature, Carbon. 48 (2010) 31–40. doi:10.1016/j.carbon.2009.07.048.

[29] L.S. Parfen'eva, T.S. Orlova, N.F. Kartenko, N.V. Sharenkova, B.I. Smirnov, I.A. Smirnov, H. Misiorek, A. Jezowski, T.E. Wilkes, K.T. Faber, Thermal conductivity of high-porosity biocarbon preforms of beech wood, Phys. Solid State. 52 (2010) 1115–1122. doi:10.1134/S1063783410060028.

[30] S.-S. Tzeng, Y.-G. Chr, Evolution of microstructure and properties of phenolic resin-based carbon/carbon composites during pyrolysis, Mater. Chem. Phys. 73 (2002) 162–169. doi:10.1016/S0254-0584(01)00358-3.

[31] A.G. Pandolfo, A.F. Hollenkamp, Carbon properties and their role in supercapacitors, J. Power Sources. 157 (2006) 11–27. doi:10.1016/j.jpowsour.2006.02.065.

[32] H. Takagi, K. Maruyama, N. Yoshizawa, Y. Yamada, Y. Sato, XRD analysis of carbon stacking structure in coal during heat treatment, Fuel. 83 (2004) 2427–2433. doi:10.1016/j.fuel.2004.06.019.

[33] F. Smits, Measurement of sheet resistivities with the four-point probe, Bell Syst. Tech. J. 37 (1958) 711–718.

[34] W.-T. Tsai, S.-C. Liu, H.-R. Chen, Y.-M. Chang, Y.-L. Tsai, Textural and chemical properties of swine-manure-derived biochar pertinent to its potential use as a soil amendment, Chemosphere. 89 (2012) 198–203. doi:10.1016/j.chemosphere.2012.05.085.

[35] S. Yamauchi, Y. Kurimoto, Raman spectroscopic study on pyrolyzed wood and bark of Japanese cedar: temperature dependence of Raman parameters, J. Wood Sci. 49 (n.d.) 235–240. doi:10.1007/s10086-002-0462-1.

[36] X. Li, J. Hayashi, C.-Z. Li, FT-Raman spectroscopic study of the evolution of char structure during the pyrolysis of a Victorian brown coal, Fuel. 85 (2006) 1700–1707. doi:10.1016/j.fuel.2006.03.008.

[37] X. Li, J. Hayashi, C.-Z. Li, Volatilisation and catalytic effects of alkali and alkaline earth metallic species during the pyrolysis and gasification of Victorian brown coal. Part VII. Raman spectroscopic study on the changes in char structure during the catalytic gasification in air, Fuel. 85 (2006) 1509–1517. doi:10.1016/j.fuel.2006.01.011.

[38] Y. Zhao, D. Feng, Y. Zhang, Y. Huang, S. Sun, Effect of pyrolysis temperature on char structure and chemical speciation of alkali and alkaline earth metallic species in biochar, Fuel Process. Technol. 141, Part 1 (2016) 54–60. doi:10.1016/j.fuproc.2015.06.029.

[39] J. McDonald-Wharry, M. Manley-Harris, K. Pickering, Carbonisation of biomass-derived chars and the thermal reduction of a graphene oxide sample studied using Raman spectroscopy, Carbon. 59 (2013) 383–405. doi:10.1016/j.carbon.2013.03.033.

[40] C. Kim, S.-H. Park, J.-I. Cho, D.-Y. Lee, T.-J. Park, W.-J. Lee, K.-S. Yang, Raman spectroscopic evaluation of polyacrylonitrile-based carbon nanofibers prepared by electrospinning, J. Raman Spectrosc. 35 (2004) 928–933. doi:10.1002/jrs.1233.

[41] B. Manoj, A.G. Kunjomana, Study of stacking structure of amorphous carbon by X-ray diffraction technique, Int. J. Electrochem. Sci. 7 (2012) 3127–3134.

[42] H. Yang, R. Yan, H. Chen, D.H. Lee, C. Zheng, Characteristics of hemicellulose, cellulose and lignin pyrolysis, Fuel. 86 (2007) 1781–1788. doi:10.1016/j.fuel.2006.12.013.

[43] F. Roig, E. Dantras, J. Dandurand, C. Lacabanne, Influence of hydrogen bonds on glass transition and dielectric relaxations of cellulose, J. Phys. Appl. Phys. 44 (2011) 045403. doi:10.1088/0022-3727/44/4/045403.

[44] W. Chen, H. Yu, Y. Liu, P. Chen, M. Zhang, Y. Hai, Individualization of cellulose nanofibers from wood using high-intensity ultrasonication combined with chemical pretreatments, Carbohydr. Polym. 83 (2011) 1804–1811. doi:10.1016/j.carbpol.2010.10.040.

[45] M. Jonoobi, J. Harun, M. Mishra, K. Oksman, Chemical composition, crystallinity and thermal degradation of bleached and unbleached kenaf bast (Hibiscus cannabinus) pulp and nanofiber, BioResources. 4 (2009) 626–639.

[46] S. Hokkanen, E. Repo, T. Suopajärvi, H. Liimatainen, J. Niinimaa, M. Sillanpää, Adsorption of Ni(II), Cu(II) and Cd(II) from aqueous solutions by amino modified nanostructured microfibrillated cellulose, Cellulose. 21 (2014) 1471–1487. doi:10.1007/s10570-014-0240-4.

[47] H. Yang, R. Yan, H. Chen, C. Zheng, D.H. Lee, D.T. Liang, In-Depth Investigation of Biomass Pyrolysis Based on Three Major Components: Hemicellulose, Cellulose and Lignin, Energy Fuels. 20 (2006) 388–393. doi:10.1021/ef0580117.

[48] M. Jonoobi, A. Khazaeian, P.M. Tahir, S.S. Azry, K. Oksman, Characteristics of cellulose nanofibers isolated from rubberwood and empty fruit bunches of oil palm

using chemo-mechanical process, Cellulose. 18 (2011) 1085–1095. doi:10.1007/s10570-011-9546-7.

[49] M.F. Rosa, E.S. Medeiros, J.A. Malmonge, K.S. Gregorski, D.F. Wood, L.H.C. Mattoso, G. Glenn, W.J. Orts, S.H. Imam, Cellulose nanowhiskers from coconut husk fibers: Effect of preparation conditions on their thermal and morphological behavior, Carbohydr. Polym. 81 (2010) 83–92. doi:10.1016/j.carbpol.2010.01.059.

[50] H. Lu, Y. Gui, L. Zheng, X. Liu, Morphological, crystalline, thermal and physicochemical properties of cellulose nanocrystals obtained from sweet potato residue, Food Res. Int. 50 (2013) 121–128. doi:10.1016/j.foodres.2012.10.013.

[51] C. Eyholzer, N. Bordeanu, F. Lopez-Suevos, D. Rentsch, T. Zimmermann, K. Oksman, Preparation and characterization of water-redispersible nanofibrillated cellulose in powder form, Cellulose. 17 (2010) 19–30. doi:10.1007/s10570-009-9372-3.

[52] C.E. Brewer, V.J. Chuang, C.A. Masiello, H. Gonnermann, X. Gao, B. Dugan, L.E. Driver, P. Panzacchi, K. Zygourakis, C.A. Davies, New approaches to measuring biochar density and porosity, Biomass Bioenergy. 66 (2014) 176–185. doi:10.1016/j.biombioe.2014.03.059.

[53] J. Lehmann, Biochar for Environmental Management: Science and Technology, Earthscan, 2012.

[54] A.K. Kercher, D.C. Nagle, Microstructural evolution during charcoal carbonization by X-ray diffraction analysis, Carbon. 41 (2003) 15–27. doi:10.1016/S0008-6223(02)00261-0.

[55] R.A. Brown, A.K. Kercher, T.H. Nguyen, D.C. Nagle, W.P. Ball, Production and characterization of synthetic wood chars for use as surrogates for natural sorbents, Org. Geochem. 37 (2006) 321–333. doi:10.1016/j.orggeochem.2005.10.008.

[56] M.F. Ashby, T. Evans, N.A. Fleck, J.W. Hutchinson, H.N.G. Wadley, L.J. Gibson, Metal Foams: A Design Guide, Elsevier, 2000.

[57] M.F. Ashby, A. Evans, N.A. Fleck, L.J. Gibson, J.W. Hutchinson, H.N.G Wadley, F. Delale, Metal Foams: A Design Guide, Applied Mechanics Reviews, 54 (2001) 105.

[58] T.D. Burchell, Carbon Materials for Advanced Technologies, Elsevier, 1999.

[59] M. Keiluweit, P.S. Nico, M.G. Johnson, M. Kleber, Dynamic Molecular Structure of Plant Biomass-Derived Black Carbon (Biochar), Environ. Sci. Technol. 44 (2010) 1247–1253. doi:10.1021/es9031419.